JOURNAL OF SOLID STATE CHEMISTRY 120, 175–181 (1995)

Ordered La(Sr)-Deficient Nonstoichiometry in $La_{0.8}Sr_{0.2}MnO_3$ Observed by High-Resolution Transmission Electron Microscopy

H. Cerva

Siemens AG, Research Laboratories, Otto Hahn Ring 6, D-81730 Munich, Germany

Received January 17, 1995; revised August 3, 1995; accepted August 7, 1995

High-resolution transmission electron microscopy (HREM) was used to identify a La(Sr)-deficient ordered nonstoichiometry in perovskite-like $La_{0.8}Sr_{0.2}MnO_3$ which is used in solid oxide fuel cell technology. Experimental 400 kV HREM images were recorded in the crystal projections ⟨112⟩ and ⟨110⟩ with the objective lens defocused to $\Delta f = -40$ nm and $\Delta f = -185$ nm. They show very good agreement with simulated images which are based on an ideal perovskite structure with 12.5 ± 5% of the La(Sr) atoms being deficient on every second {111} plane. The actual rhombohedral distortion of $La_{0.8}Sr_{0.2}MnO_3$ alone, as determined by X-ray diffraction, is not responsible for the observed HREM image contrasts. In addition, possible ordering of the strontium atoms could be excluded with the help of image simulations. © 1995 Academic Press, Inc.

1. INTRODUCTION

Lanthanum strontium manganate with its pseudocubic perovskite structure has interesting magnetic and electronic properties (1). In particular $La_{0.8}Sr_{0.2}MnO_3$ may be used as an electrode in high-temperature solid oxide fuel cells (SOFC) (2–4). Lanthanum manganate is well known for its oxygen nonstoichiometry arising under oxidative conditions which leads to interstitial oxygen ($LaMnO_{3+\delta}$). Charge compensation is achieved via oxidation of the Mn ions while a stoichiometric Mn-cation and O-anion sublattice results from the formation of both a second phase (La_2O_3) and La vacancies to form $La_{1-x}MnO_3$ (5). In this work the $La_{0.8}Sr_{0.2}MnO_3$ samples are calcined at 1200°C by mixing La_2O_3, $SrCO_3$, and MnO_2 powders. These powders are mixed with an organic system and screen printed and sintered onto an 8% Yttria-stabilized ZrO_2 (8YSZ) substrate at 1300°C for 5 hr in air. The thin $La_{0.8}Sr_{0.2}MnO_3$ layers serve as cathodes on the 8YSZ-electrolyte for SOFC cell applications. During SOFC cell operation at 950°C the cathode is exposed to oxygen. Irrespective of whether the material is only calcined or additionally sintered onto the 8YSZ substrate or is further used in an operating SOFC cell, the $La_{0.8}Sr_{0.2}MnO_3$ grains show a superstructure which manifests itself in 1/2{111} electron diffraction spots and in the high-resolution transmission electron microscopy (HREM) image contrast of both ⟨112⟩ and ⟨110⟩ projections (because of simplicity cubic indices are used although the crystal structure is rhombohedral). In a recent paper the HREM image contrast of particular planar La(Sr)-vacancy defects on {100} planes of such $La_{0.8}Sr_{0.2}MnO_3$ grains was described (6). Since the publication of that work it was found that these planar defects appear only after the SOFC cell was operated. In this paper attention is given to the superstructure observed in the HREM images. Comparisons of experimental and simulated images explain the contrast to be due to an ordered La(Sr)-deficient nonstoichiometry of $La_{0.8}Sr_{0.2}MnO_3$.

2. EXPERIMENTAL

The solid solution $La_{0.8}Sr_{0.2}MnO_3$ samples were produced according to the conventional mixed oxide method, i.e., by a solid state reaction between oxides (La_2O_3, MnO_2) and, in the case of strontium, the carbonate. After a separate milling process of La_2O_3, desired ratios of all raw materials were weighed in and homogenized together in a ball mill. A calcination step followed at 1200°C in air with a holding time of 10 hr in an aluminumoxide crucible. For the production of cathode layers on the 8YSZ electrolyte substrate, these powders were mixed with an organic binder system (60 wt% of powder) and screen printed onto the substrate. The cathode layer was sintered onto the substrate at 1300°C/5 hr in air. For electrical SOFC measurements, the cathode was operated at 950°C under O_2 (dynamic flow) at current densities up to 1 A/cm^2 and cell voltages between 1.2 and 0.7 V (7).

HREM was carried out in a JEOL 4000EX microscope operated at 400 kV. The EMS programs of Stadelmann (8) were used to calculate high-resolution multislice images with the following microscope parameters: spherical aberration constant $C_S = 1$ mm, defocus spread $\Delta = 13$ nm, semi-convergence angle $\alpha = 0.9$ mrad, and objective lens aperture diameter 20 nm^{-1}. TEM specimens were prepared by mechanical grinding and conventional Ar-ion beam thinning with 3 kV, 10° incidence angle, and liquid nitrogen

0022-4596/95 $12.00

cooling. The objective lens defoci at which the experimental HREM images were recorded were determined from the image of the thin amorphous edge of the specimen either by using optical diffraction patterns (9) or fast-Fourier transformations of the digitized image (10). From such a reciprocal image the zeros of the contract transfer function and thus the objective lens defocus at which the HREM image was recorded may be deduced (9). In particular, large defoci were estimated before taking a photograph by counting the number of calibrated objective lens focus steps when starting from a known reference value. This reference value is the defocus value where the amorphized edge of the specimen appears with minimum contrast. For the given TEM this is $\Delta f = -20$ nm.

3. STRUCTURAL CONSIDERATIONS

3.1. The Structure of Lanthanum Strontium Manganate

$La_{0.8}Sr_{0.2}MnO_3$ is trigonal (R-3c, spacegroup 167) at room temperature and may be described with a pseudocubic cell $a = 0.387$ nm, $\alpha = 89.55°$ as determined with X-ray powder diffraction (11, 12).

The following structure is obtained for $LaMnO_{3.12}$ under an oxidizing ambient (5): on the basis of X-ray diffraction analysis it was indexed with a primitive rhombohedral cell having the unit cell parameters $a_r = 0.5471$ and $\alpha_r = 60.66°$. The angle $\alpha_r = 60°$ corresponds to an ideal undistorted perovskite structure. The analyzed structure can be envisaged as consisting of eight distorted perovskite unit cells yielding a pseudocubic unit cell with a doubled perovskite lattice parameter $a = 0.7776$ nm. The distortion occurs from the rotation of the BO_6 octahedra around a cubic ⟨111⟩ axis which causes neighboring octahedra to rotate in opposite directions. Thus a distorted perovskite cell with a doubled perovskite lattice parameter $a = 0.7776$ nm is produced. Atom positions were determined by neutron diffraction and the best agreement was obtained with spacegroup R-3c for cation-understoichiometric $La_{0.94}Mn_{0.98}O_{3.00}$ which forms from $LaMnO_{3.12}$ by the reaction (5)

$$LaMnO_{3.12} \rightarrow 0.02\,La_2O_3 + \underset{(La_{0.96}MnO_{3.06} \equiv La_{0.94}Mn_{0.98}O_{3.00})}{La_{0.96}MnO_{3.06}} \quad [1]$$

If lanthanum is substituted by strontium in the range $0 \leq x \leq 0.45$, then the rhombohedral angle α_r and the hexagonal lattice parameter a_h, respectively, decrease with increasing strontium content x (12). This indicates that an increasing Sr content reduces the distortion of the ideal perovskite structure. $La_{1-x}Sr_xMnO_3$ exhibits a phase transition from rhombohedral to cubic at the transition temperature T_C which depends on the Sr content x. This was verified by high temperature X-ray diffraction (11): For $x = 0.2$ the transition temperature is $T_C = 1235°C$, whereas for $x = 0.5$ the transition temperature is much lower: $T_C = 180°C$.

In this work the HREM contrast of thin specimens of $La_{0.8}Sr_{0.2}MnO_3$ is described with the ABO_3 perovskite structure (space group 221) $a = 0.386$ nm because the HREM images are assumed to be not sensitive enough in first order to the lattice distortions of the perovskite cell. For comparison also the rhombohedral structure determined by Tofield and Scott (5) for lanthanum manganate will be considered which shows the largest distortion from the ideal perovskite structure.

3.2. TEM Diffraction Patterns

The TEM diffraction patterns in Figs. 1a–1c are cubically indexed and show [-101], [-1-12], and [0-11] poles of the same grain. In both ⟨112⟩ and ⟨110⟩ poles additional 1/2{111} diffraction spots, their odd multiples, and vectorially added spots 1/2{111} + n{100}, 1/2{111} + n{011} appear. In the ideal perovskite structure they are kinematically forbidden in both types of poles. In the rhombohedral structure (R-3c, atom positions from (5)) these diffraction spots are also kinematically forbidden in those poles which correspond to the cubic ⟨110⟩ poles. However, in the rhombohedral poles corresponding to the cubic ⟨112⟩ pole only the diffraction spots corresponding to the cubic diffraction spots $(2n + 1)/2${111} are kinematically forbidden. The appearance of these spots in the rhombohedral ⟨112⟩ poles may be explained by Umweganregung. It will be shown later that all of these diffraction spots may be explained by a structural model which takes into account the ordering of La(Sr)-deficient atom positions. As mentioned in the Introduction these additional 1/2{111} may be observed in the calcinated or sintered grains, as well as in those grains which were operated in a SOFC cell.

3.3. Stoichiometric $La_{0.8}Sr_{0.2}MnO_3$ with the Ideal Perovskite Structure

Figure 2a shows the structure of $La_{0.8}Sr_{0.2}MnO_3$ in the ⟨110⟩ projection. In the in-plane ⟨100⟩ direction La(Sr)/O and Mn/O planes alternate. The La(Sr)/O plane consists of atom columns each of which is alternately occupied by La(Sr) and O atoms. The sequence of La(Sr) and O atoms in adjacent atom columns is displaced by half a period. In the Mn/O plane pure Mn and O columns lie next to each other. Various spacings of lattice planes are indicated in the figure. The HREM work in (6) has shown that the La(Sr)/O columns appear as dark dots while the tunnel regions between reveal a characteristic bright dumb-bell contrast for TEM specimen thicknesses $t \leq 3$ nm and objective lens defoci -45 nm $\leq \Delta f \leq -35$ nm (for the same microscope as used in this work).

The ⟨112⟩ projection is displayed in Fig. 2b. In the in-

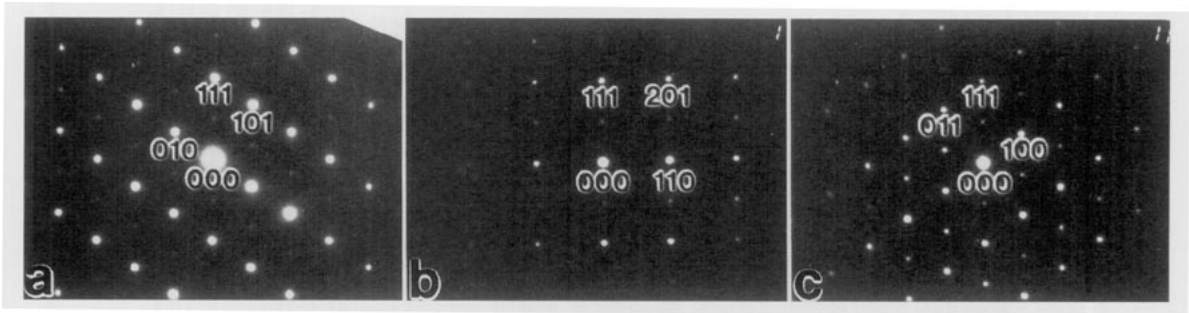

FIG. 1. Electron diffraction patterns of one $La_{0.8}Sr_{0.2}MnO_3$ grain. The three poles were obtained by tilting the grain around a ⟨111⟩ axis over 60° (cubic indices). (a) [-101], (b) [-1-12], (c) [0-11] poles.

plane ⟨111⟩ direction La(Sr)/O and Mn planes alternate. The spacing between two La(Sr)/O or two Mn planes corresponds to the {111} lattice spacing. The La(Sr)/O plane consists of mixed La(Sr)/O and pure O columns whereas the Mn plane is made up of Mn columns only. The experimental HREM contrast will be discussed below.

3.4. *Nonstoichiometric $(La_{0.8}Sr_{0.2})_yMnO_3$ with an Ordered La(Sr)-Deficient Sublattice in the Perovskite Structure*

A structural model has been conceived which assumes on all four equivalent {111} planes of the perovskite structure a deficiency in the occupancy $(2y - 1)$ of the La(Sr) positions on every second {111} plane. The perovskite unit cell parameter is thus doubled (a = 0.772 nm) and the chemical formula is $(La_{0.8}Sr_{0.2})_yMnO_3$. Each La(Sr) position with occupancy 1 is surrounded by six next La(Sr) positions having an occupancy of $(2y - 1)$.

The ⟨110⟩ projection of $(La_{0.8}Sr_{0.2})_yMnO_3$ in Fig. 2c displays a superstructure on both {111} planes (every second {111} plane has a lower La(Sr) occupancy). In the in-plane ⟨100⟩ direction this causes alternating $La(Sr)_1/O$ and $La(Sr)_{(2y-1)}/O$ columns within the La(Sr)/O planes. Therefore, this projection should yield a contrast difference at these positions in the HREM images.

The ⟨112⟩ projection of $(La_{0.8}Sr_{0.2})_yMnO_3$ in Fig. 2d exhibits alternating $La(Sr)_1/O$ and $La(Sr)_{(2y-1)}/O$ planes which should also become distinguishable in the HREM image.

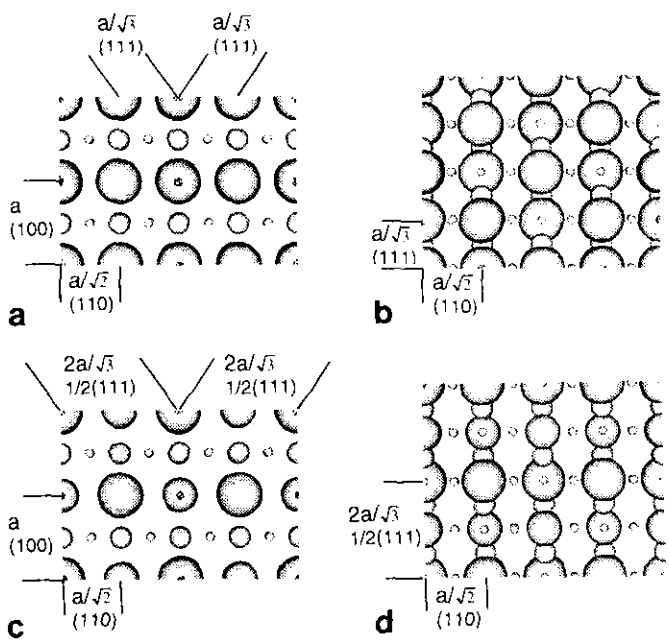

FIG. 2. Structural models of stoichiometric $La_{0.8}Sr_{0.2}MnO_3$ with the ideal perovskite structure in the (a) ⟨110⟩ and (b) ⟨112⟩ projections; Nonstoichiometric $(La_{0.8}Sr_{0.2})_yMnO_3$ with the La(Sr)-deficient atom positions ordered on every second {111} plane in the (c) ⟨110⟩ and (d) ⟨112⟩ projections. (Atom positions: large circles, La(Sr) with occupancy $y = 1$; medium circles, La(Sr) with occupancy $(2y - 1)$; small circles, Mn; very small circles, O.)

4. HIGH-RESOLUTION TEM

4.1. *The ⟨112⟩ Projection*

Figure 3 displays simulated images of $(La_{0.8}Sr_{0.2})_yMnO_3$ in the stoichiometry range $0.75 \leq y \leq 1$ calculated for specimen thicknesses $1 \leq t \leq 9$ nm at an objective defocus $\Delta f = -40$ nm. In stoichiometric material ($y = 1$) the high-resolution contrast exhibits the following features for $t \leq 7$ nm: the horizontal rows of black dots correspond to the {111} planes occupied by La(Sr)/O and O columns with the La(Sr)/O columns at the center of the black dots. The Mn columns lie in the horizontal rows of bright dots, centered between adjacent bright dots. This contrast behavior is stable in the range $-50 \leq \Delta f \leq -30$ nm as verified by simulations. When inspecting Fig. 3 it becomes apparent that every second horizontal row of black dots becomes brighter for decreasing values of y. This is in particular true for $t \leq 5$ nm. Figure 4 shows an experimental ⟨112⟩ HREM image recorded at $\Delta f = -40$ nm (The optical diffraction pattern was recorded from the amorphous rim of the specimen). In every second horizontal row there is increased intensity at the position of the black dots. The upper inset shows the projected structure ($y = 1$) and thus

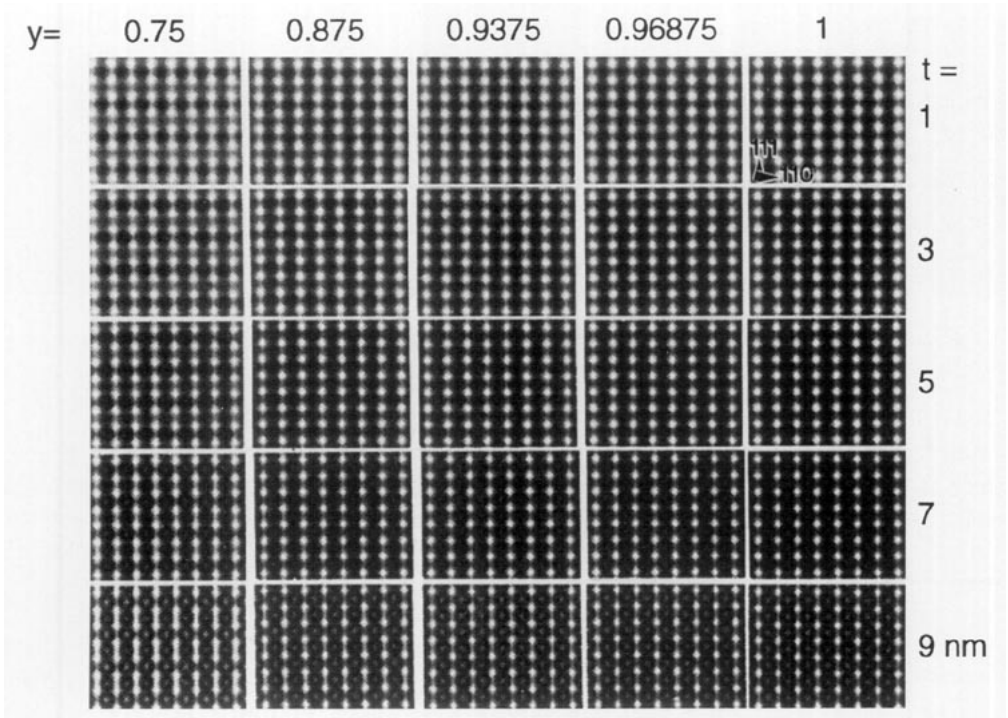

FIG. 3. ⟨112⟩ projected HREM images of $(La_{0.8}Sr_{0.2})_yMnO_3$ calculated for $0.75 \leq y \leq 1$, specimen thicknesses $1 \leq t \leq 9$ nm, and $\Delta f = -40$ nm.

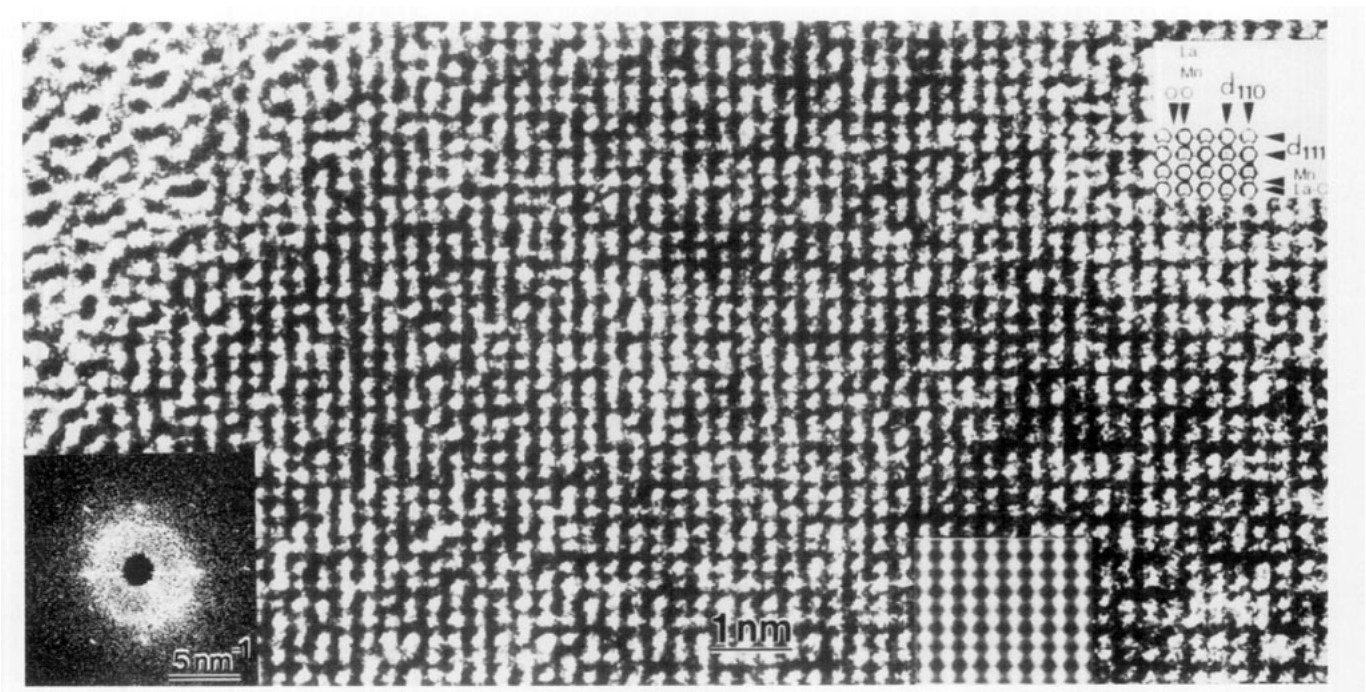

FIG. 4. Experimental ⟨112⟩ HREM image of $La_{0.8}Sr_{0.2}MnO_3$ recorded at $\Delta f = -40$ nm. The inset in the lower middle part of the figure shows a simulated image ($y = 0.875$, $t = 3$ nm). The inset in the top right corner displays the correlation between projected atom positions and image contrast (compare with Fig. 2b). The inset in the bottom left corner is the optical diffractogram obtained from the thin amorphous edge of the specimen and was used to determine the objective lens defocus.

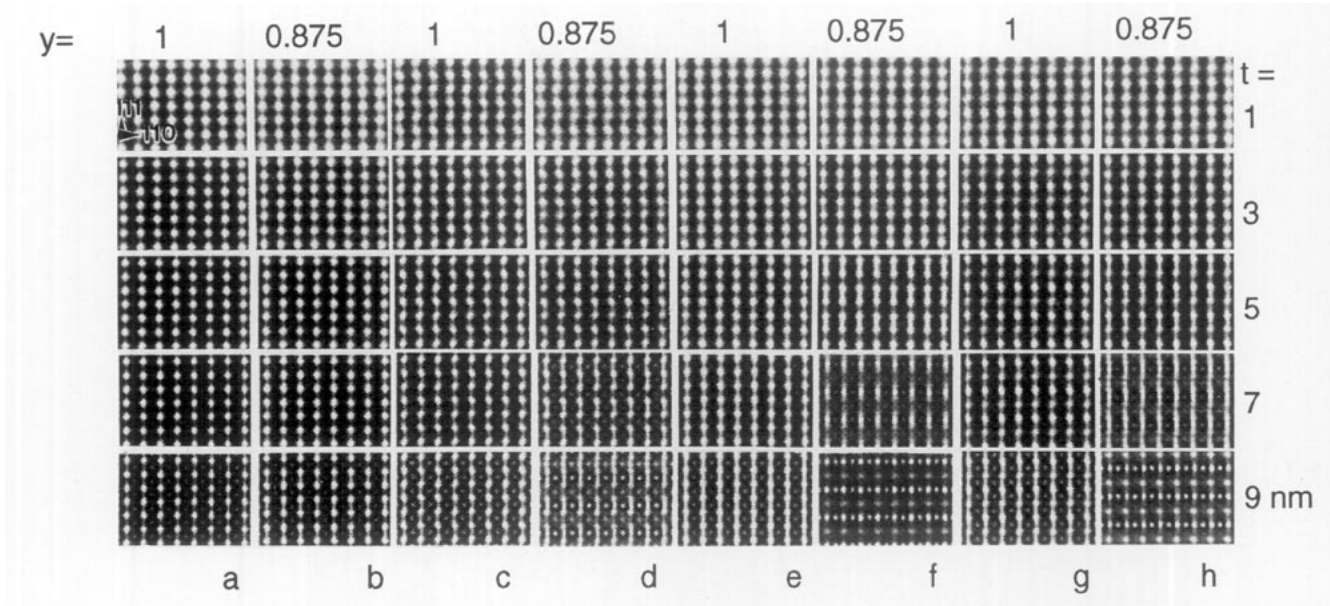

FIG. 5. Calculated ⟨112⟩ HREM images of $(La_{0.8}Sr_{0.2})_yMnO_3$ with (a and b) the idel perovskite structure and (c–h) the rhombohedrally distorted structure for $\Delta f = -40$ nm, $y = 0.875$ and $y = 1$ in the thickness range $1 \leq t \leq 9$ nm. (a, b) ⟨112⟩; (c, d) ⟨01.0⟩; (e, f) ⟨10.2⟩; and (g, h) ⟨21.1⟩ projections.

the correlation between the atom positions and the image contrast. The lower inset is a simulated image from the table in Fig. 3 which shows the best fit to the experimental image. This suggests a La(Sr) deficiency of 12.5% ($y = 0.875$).

In order to make sure that the observed HREM contrast is not simply due to the rhombohedral distortion of the perovskite structure, image simulations were carried out for the rhombohedral structure using the atom positions given in Ref. (5). Figure 5 compares simulated images of the perovskite ⟨112⟩ projection with the corresponding three nonequivalent rhombohedral projections (hexagonal Miller–Bravais indices) for the parameters $1 \leq t \leq 5$ nm, $\Delta f = -40$ nm, and $y = 0.8745$ and 1. Though the shape of the bright dots, particularly for the $\langle 10.1 \rangle_h$ projection in Figs. 5c and 5d, is slightly different from the ideal structure (Figs. 5a and 5b), the black dots in every second horizontal row become less intense for $y = 0.875$ in all cases. Therefore, it is ruled out that the distorted perovskite structure is responsible for the observed HREM contrast in Fig. 4.

4.2. The ⟨110⟩ Projection

A detailed description of the HREM image contrast in ⟨110⟩ projection for $y = 1$ and $\Delta f = -40$ nm was given in Ref. (6). A defocus of -40 ± 10 nm was suitable to identify defects on {100} planes as La(Sr)-vacancy precipitates. Though 1/2{111} diffraction spots were observed in the diffraction patterns of the ⟨110⟩ pole, the image contrast for $\Delta f = -40$ nm did not reveal pronounced features which could be attributed to an ordered La(Sr) deficiency. Hence, imaging conditions were sought showing a strong contrast of the 1/2{111} periodicities. Figure 6 shows an experimental high-resolution image, recorded close to $\Delta f = -185$ nm (the optical diffraction pattern was recorded from the amorphous rim of the specimen to determine the defocus), where the 1/2{111} periodicities are strongly pronounced. The insets are calculated images of the nonstoichiometric material ($y = 0.875$) with the ideal perovskite structure for the thicknesses $t = 3$, 5, and 10 nm. Figures 7a and 7b compare simulated images in the ⟨110⟩ projection with the ideal perovskite structure for $y = 1$ and $y = 0.875$ at a defocus $\Delta f = -185$ nm, and in the thickness range $1 \leq t \leq 10$ nm. The 1/2{111} periodicities are only present in the images calculated for the ordered La(Sr)-deficient nonstoichiometric material ($y = 0.875$) at $t \geq 5$ nm. Image simulations revealed that this contrast is stable in the focus range $-190 \leq \Delta f \leq -180$ nm. The stoichiometric model, however, cannot explain the contrast observed experimentally in Fig. 6. The large black dots in the images of Fig. 7b at $t = 10$ nm correspond to the La(Sr)/O columns with La(Sr) deficiencies. The calculations carried out for the equivalent rhombohedral projections ⟨2-1.0⟩ and ⟨0-1.1⟩ are displayed in Figs. 7c–7f. Distinct 1/2{111} periodicities are only visible for $y = 0.875$ and the contrast patterns resemble those calculated for the ideal perovskite structure with $y = 0.875$. However, similar images appear at slightly different specimen thicknesses.

5. DISCUSSION

The structural model of $(La_{0.8}Sr_{0.2})_yMnO_3$ with the La(Sr)-deficient positions ordered on every second {111}

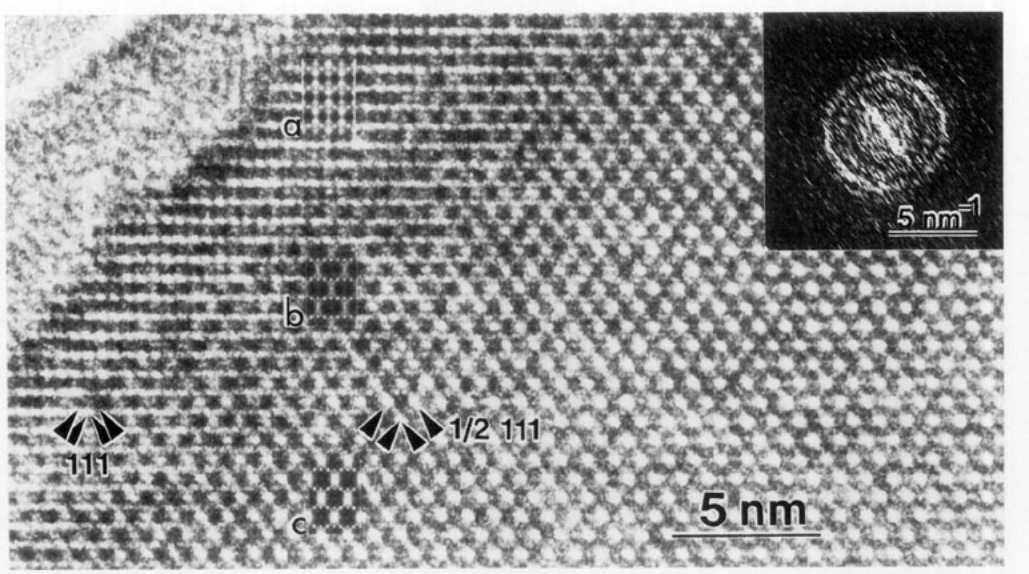

FIG. 6. Experimental ⟨110⟩ HREM image of $La_{0.8}Sr_{0.2}MnO_3$ recorded at $\Delta f = -185$ nm. The insets (a–c) are the best fit of simulated images for the ideal perovskite structure ($y = 0.875$, t = (a) 3, (b) 5, (c) 10 nm). The inset in the top right corner is a fast-Fourier transformed image obtained from the thin amorphous edge of the specimen and was used to determine the objective lens defocus.

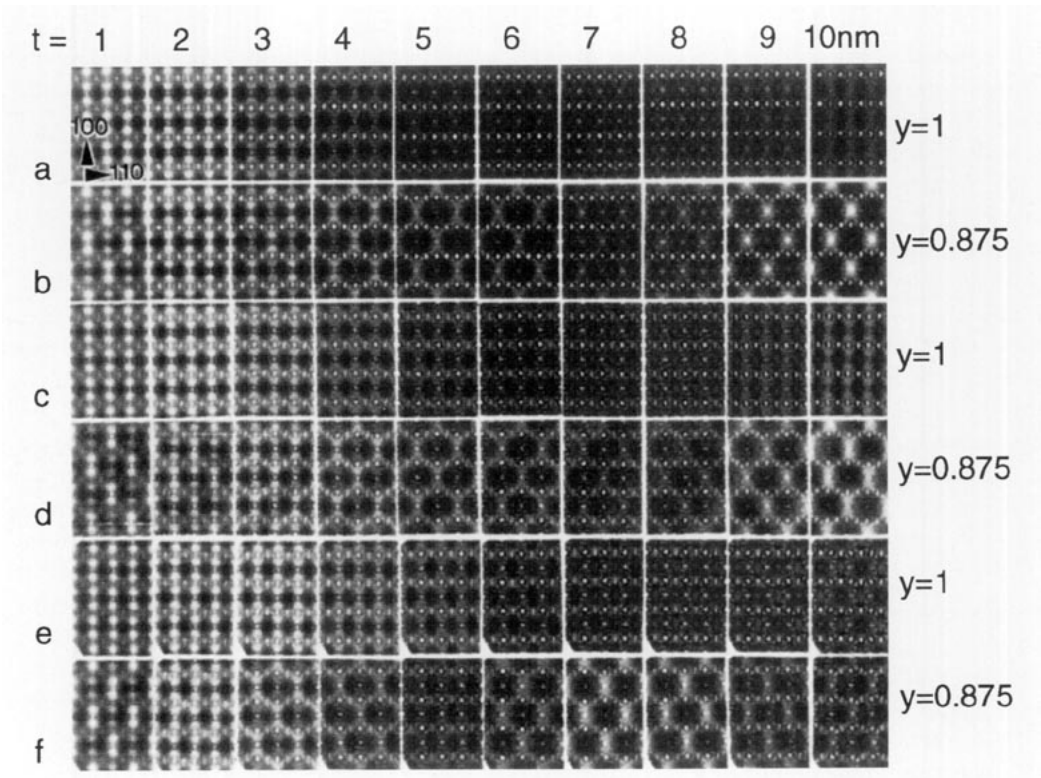

FIG. 7. Calculated HREM images for $\Delta f = -185$ nm in the thickness range $1 \leq t \leq 10$ nm. Ideal Perovskite structure in the ⟨110⟩ projection with La(Sr) occupation (a) $y = 1$ and (b) $y = 0.875$; rhombohedrally distorted structure in the ⟨2-1.0⟩ projection with La(Sr) occupation (c) $y = 1$ and (d) $y = 0.875$; in the ⟨0-1.1⟩ projection with La(Sr) occupation (e) $y = 1$ and (f) $= 0.875$.

plane explains the observed HREM image contrasts in both ⟨112⟩ and ⟨110⟩ projections. The intensities in the experimental images were qualitatively compared with those in the simulated images of the structural model given in Section 3.4 for various occupations y. A La(Sr) deficiency of 12.5 ± 5% (y = 0.875 ± 0.05) was deduced from the images by this comparison. Extensive simulations which took into account the rhombohedrally distorted perovskite lattice revealed that the observed 1/2{111} superstructure visible in the HREM images is not due to this structural distortion. Thus, it is sufficient to describe the experimental HREM images with the help of a model with cubic structure in this first approach, although the structure will be rhombohedrally distorted (11, 12). Also, the case for an ordering of the Sr atoms was considered: in this case the {111} planes were successively occupied by pure La/O and $La_{0.6}Sr_{0.4}$/O planes. Contrast changes were observed neither in the ⟨112⟩ nor in the ⟨110⟩ projection.

The identification of the ordered La(Sr)-deficient nonstoichiometry of $La_{0.8}Sr_{0.2}MnO_3$ for a particular condition of sintering is important in order to understand the chemical reactivity of this material. Although the composition of the calcined powder is stoichiometric as proven by chemical analysis (inductively coupled plasma–mass spectroscopy) the described calcination procedure produces a superstructure in $La_{0.8}Sr_{0.2}MnO_3$ resulting from an ordered La(Sr)-deficient nonstoichiometry which is still present after sintering and/or operation of the SOFC cell. Therefore, a second phase is expected to form according to the reaction in Eq. [1]. Such a phase ($La_2Zr_2O_7$) is indeed found in cross sections by, e.g., scanning electron microscopy (13). It has been mentioned in the Introduction that the planar La(Sr)-vacancy defects on the {100} planes reported earlier (6) are only observed after operating the SOFC cell. Obviously both the high operation temperature of the SOFC cell at 950°C and the electron current through the material lead to a further depletion of the La(Sr) content in the material by the additional formation of these planar defects. From the defect density a reduction of the La(Sr) content by approximately 1% is estimated (6). This amount of lanthanum is assumed to diffuse into and react with the electrolyte.

6. CONCLUSION

A superstructure with 1/2{111} spacings was observed in the contrast of ⟨112⟩ and ⟨110⟩ HREM images of $La_{0.8}Sr_{0.2}MnO_3$. Simulated HREM images based on a model with cubic structure may explain the HREM contrast to originate from an ordered La(Sr) deficiency on every second {111} plane on each set of {111} lattice planes. Although the structure is trigonal as determined by X-ray diffraction (5, 11, 12) it may be derived from a cubic structure by a rhombohedral distortion. This deviation from the cubic structure alone, however, may not explain the observed HREM image contrast. Also an ordering of the La and Sr atoms may be excluded. HREM image simulations of $(La_{0.8}Sr_{0.2})_yMnO_3$ with different deficiencies and comparison with the experimental images yield y = 0.875 ± 0.05. The finding of this cation nonstoichiometry is important for the understanding of the material reactions between lanthanum strontium manganate and zirconium oxide in solid oxide fuel cell technology.

ACKNOWLEDGMENTS

The author thanks R. Männer for providing the sample, M. Schiele for TEM specimen preparation, T. Fuska for photographic work, and H. Oppolzer for a critical reading of the manuscript. H.C. is also indebted to R. Ziel and O. Greis for providing the FFT image in Fig. 6.

REFERENCES

1. F. S. Galasso, "Perovskites and High-T_C Superconductors." Gordon and Breach, New York, 1990.
2. B. C. H. Steele, "Bulletin of the Materials Research Society," p. 19. Materials Research Society, Pittsburgh, 1989.
3. E. Ivers-Tiffeé, W. Wersing, M. Schießl, and H. Greiner, *Ber. Bunsenges. Phys. Chem.* **94,** 978 (1990).
4. A. Hammouche, E. J. L. Schouler, and M. Henault, *Solid State Ionics* **28–30,** 1205 (1988).
5. B. C. Tofield and W. R. Scott, *J. Solid State Chem.* **10,** 183 (1974).
6. H. Cerva, *J. Solid State Chem.* **114,** 211 (1995).
7. M. Schießl, E. Ivers-Tiffeé, and W. Wersing, *in* "Ceramics Today - Tomorrow's Ceramics", (Vincenzini, Ed.), p. 2607. Elsevier, Amsterdam, 1991.
8. P. A. Stadelmann, *Ultramicroscopy* **21,** 131 (1987).
9. O. L. Krivanek, *Optik* **45,** 97 (1976).
10. CRISP-Image processing of electron micrographs by S. Hovmöller, Calidris Inc., Manhemsvägen 4, S-19146 Sollentuna, Sweden.
11. A. Iberl, Diploma Thesis, University Regensburg, Germany, 1991.
12. A. Hammouche, E. Siebert, and A. Hammou, *Mater. Res. Bull.* **24,** 367 (1989).
13. J. A. M. van Roosmalen and E. H. P. Cordfunke, *Solid State Ionics* **52,** 303 (1992).